

PAPER

Time evolution of CO₂ ro-vibrational excitation in a nanosecond discharge measured with laser absorption spectroscopy

To cite this article: Yanjun Du *et al* 2021 *J. Phys. D: Appl. Phys.* **54** 365201

View the [article online](#) for updates and enhancements.



IOP | ebooks™

Bringing together innovative digital publishing with leading authors from the global scientific community.

Start exploring the collection—download the first chapter of every title for free.

Time evolution of CO₂ ro-vibrational excitation in a nanosecond discharge measured with laser absorption spectroscopy

Yanjun Du* , Tsanko V Tsankov , Dirk Luggenhölscher and Uwe Czarnetzki 

Institute for Plasma and Atomic Physics, Ruhr University Bochum, D-44780 Bochum, Germany

E-mail: duyanjun13@gmail.com

Received 18 February 2021, revised 23 April 2021

Accepted for publication 21 May 2021

Published 24 June 2021



Abstract

CO₂ dissociation stimulated by vibrational excitation in non-equilibrium discharges has drawn lots of attention. Nanosecond (ns) discharges are known for their highly non-equilibrium conditions. It is therefore of interest to investigate the CO₂ excitation in such discharges. In this paper, we demonstrate the ability for monitoring the time evolution of CO₂ ro-vibrational excitation with a well-selected wavelength window around 2289.0 cm⁻¹ and a single continuous-wave quantum cascade laser with both high accuracy and temporal resolution. The rotational and vibrational temperatures for both the symmetric and the asymmetric modes of CO₂ in the afterglow of CO₂ + He ns-discharge were measured with a temporal resolution of 1.5 μs. The non-thermal feature and the preferential excitation of the asymmetric stretch mode of CO₂ were experimentally observed, with a peak temperature of $T_{v3, \max} = 966 \pm 1.5$ K, $T_{v1,2, \max} = 438.4 \pm 1.2$ K and $T_{\text{rot}} = 334.6 \pm 0.6$ K reached at 3 μs after the nanosecond pulse. In the following relaxation process, an exponential decay with a time constant of 69 μs was observed for the asymmetric stretch (001) state, consistent with the dominant deexcitation mechanism due to VT transfer with He and deexcitation on the wall. Furthermore, a synchronous oscillation of the gas temperature and the total pressure was also observed and can be explained by a two-line thermometry and an adiabatic process. The period of the oscillation and its dependence on the gas components is consistent with a standing acoustic wave excited by the ns-discharge.

Keywords: carbon dioxide dissociation, nanosecond discharge, quantum cascade laser absorption spectroscopy, vibrational and rotational temperatures

(Some figures may appear in color only in the online journal)

1. Introduction

In the last decades, CO₂ conversion is of growing interest in the context of greenhouse gas abatement and renewable energy exploration. The non-thermal plasma is a promising means for efficient conversion since the unique electron, vibrational, rotational, and gas temperatures in these plasmas

allow focusing the discharge energy to the desired channels instead of heating the gas [1, 2]. Specifically, the vibrational excitation, starting with electron-impact-excitation of lower vibrational levels, followed by vibrational–vibrational (V–V) excitation close to the dissociation threshold level, is a more efficient dissociation pathway [3, 4]. This ladder-climbing population to higher vibrational levels occurs owing to the small difference (~0.3 eV) between the higher vibrational levels and faster V–V relaxation rates compared to

* Author to whom any correspondence should be addressed.

vibrational–translational (V–T) transfer. The electron energy required for vibrational dissociation, which equals the O=CO bond energy (5.5 eV), is much lower than that of the direct electron-impact dissociation (>7 eV).

However, the detailed physical mechanisms of the vibrational excitation stimulated dissociation are fairly complex. Related questions involve the excitation mechanism by electrons, including interaction of electrons with excited states by superelastic collisions, excitation transfer within one species, e.g. CO₂ with CO₂, and excitation transfer between different molecules, e.g. N₂ with CO₂. Significant effort has been made to investigate this process both numerically [5–8] and experimentally [9–12]. The temporally resolved measurement of CO₂ ro-vibrational excitation is of great importance to gain insight into the excitation and relaxation processes and also the validation of the detailed kinetic modeling of CO₂ dissociation.

Different optical diagnostic methods have been used to investigate the CO₂ excitation/relaxation process in various types of discharges, e.g. Raman scattering [11–13] and IR emission [14, 15]. However, the former gives only limited information about the Raman active symmetric bending and stretching modes and the latter presents only qualitative information due to the strong self-absorption. Compared to them, IR absorption spectroscopy is a powerful method that is suitable for this topic. Particularly, broadband IR light sources in combination with Fourier transform infrared spectroscopy (FTIR) provide a relatively large scan range, and thus ensure a simultaneous detection of multiple vibrational modes and even multiple species [16–18]. Rivallan *et al* [16] have demonstrated the possibility of detecting the temporally resolved CO₂ absorption spectrum with step-scan acquisition mode of FTIR in a CO₂/air glow discharge. Klarenaar *et al* [17] further developed a fitting approach to deduce the multiple vibrational temperatures and CO₂ number density from the broadband absorption spectrum from FTIR. Being able to provide a whole picture of the CO₂ excitations in all three vibrational modes, time-resolved FTIR has been widely applied to investigate CO₂ dissociation in pulsed DC glow discharges [18] and radio-frequency (RF) discharges [19–21].

Despite all these attractive advantages, the accuracy and the sensitivity to vibrational temperatures of FTIR are still limited due to the large instrument broadening. Specifically, since the detected absorbance is a convolution of the real absorbance with large instrument broadening, the detected absorbance from FTIR is in fact spectrally ‘smoothed’ and averaged, which results in the following effects: (a) the real absorption is generally too strong, even saturated, making the detected absorbance less sensitive to the gas properties (temperature and concentration) considering the exponential relationship in the Beer–Lambert Law; (b) the small absorption peaks from higher vibrational states, that are essential for the vibrational temperature determination, are always obscured in the final smoothed spectrum, making this method not sensitive to the important vibrational temperature even at low pressure.

The recently developed quantum cascade laser (QCL), especially the fast frequency chirp of pulsed QCLs, known as the *intrapulse* mode [22], makes it possible to probe the

time-resolved absorption spectrum [23–25]. More recently, Damen *et al* [26, 27] proposed to measure the time evolution of CO₂ excitation with the intermittent scanning of three QCLs operated in pulsed mode with a temporal resolution of $\sim 100 \mu\text{s}$. With decent efforts to avoid the rapid passage effects [28, 29] and jitter [30], which are the inherent defects of this *intrapulse* operation mode, improved accuracy and sensitivity to vibrational temperature were achieved compared to FTIR. However, further improvement in the temporal resolution is challenging due to the compromise between the total scan range and the ultimate temporal resolution (laser pulse length). It is generally limited to the order of tens of μs estimated with a downchirp rate of several MHz ns^{-1} and a scan range of $\sim 1 \text{ cm}^{-1}$ to cover enough transitions from different vibrational modes of CO₂, although it varies with lasers. In addition, the measurement accuracy of absorbance is strongly subject to the pulse to pulse fluctuations in both laser intensity and chirp rate [25].

In this work, the nanosecond pulsed discharge, which enables a good separation and control of the electron excitation and the collisional ro-vibrational excitation, will be used to investigate the CO₂ vibrational excitation. To achieve both high accuracy and temporal resolution, a method is applied with a well-selected wavelength window and a single QCL operating in a continuous slow scan (or step scan) mode. With this method, rotational and multiple vibrational temperatures together with the CO₂ density are simultaneously determined with a temporal resolution of $1.5 \mu\text{s}$ and high accuracy as well. The fast excitation and relaxation process for all three vibration modes of CO₂ in the afterglow of the CO₂–He nanosecond pulsed discharge will be presented and discussed.

2. Experimental setup and measurement strategy

2.1. Nanosecond pulsed DC discharge

The experimental setup is schematically shown in figure 1(a). The nanosecond discharge used in this paper is similar to that in [31]. To be brief, the discharge consists of two molybdenum electrodes with a cross-section of $20 \times 1 \text{ mm}$ placed vertically with a distance of 1 mm. Two glass plates are pressed tightly to the electrodes at the front and the back, yielding a well-confined discharge volume of $20 \text{ mm} \times 1 \text{ mm} \times 1 \text{ mm}$. Nanosecond voltage pulse generated by combining a DC power supply (Heinzinger, LNC 6000-10 neg) with a fast high-voltage switch (Behlke HTS-81) is applied to one electrode with the other one grounded. A delay generator (Stanford Research Systems DG535) with internal triggering is used to trigger the switch with a repetition rate of $f_p = 2 \text{ kHz}$ and an on-time of 150 ns. To allow easy discharge operation, the value of the repetition frequency is chosen within a range determined by the energy input to the system (to limit gas heating) and remaining seed electrons from the previous pulse (to ease discharge ignition). The applied voltage and the current are monitored by a high-voltage probe (Lecroy PPE6kV) and a current probe (American Laser Systems, Model 711) in conjunction with an oscilloscope (Lecroy, WaveSurfer 510). The incoming gas consists of 10% CO₂ + He by mixing pure CO₂

and He gas flow using two mass flow controllers (MKS instruments) with a total flow rate of 30 sccm. The gas mixture is guided into the discharge gap through a hole in the center of the back glass plate and leaves the discharge from both ends, as shown in the inset in figure 1(a). The pressure in the discharge chamber is monitored by a pressure gauge (Pfeiffer vacuum) and is kept constant at 145 mbar by fine adjusting the mechanical needle valve at the gas outflow. At this condition, the gas residence time is around 6 ms, that ensures that all molecules experience 12 pulses before leaving the discharge. The discharge emission is visually homogeneous within the whole discharge gap, motivating the assumption that the plasma is homogeneous with spatially uniform properties. The temporal averaging in these observations is certainly a limitation, but performing a temporally resolved imaging of the discharge is beyond the scope of this paper. The shot-to-shot stability is assessed by the current and voltage waveforms, which deviate by no more than 2% between the pulses. The voltage and the current waveforms are shown in figure 1(b). Their trends in CO₂ resemble those in N₂ [32, 33] and H₂ [34] in a similar discharge setup. The figure presents also the power coupled into the discharge. At the present conditions, this amounts to about 1 mJ or about 0.9 eV per CO₂ molecule.

2.2. Optical system and measurement strategy

The laser system to probe CO₂ absorption spectrum is rather compact and simple, as shown in figure 1(a). A single-mode continuous-wave QCL (Alpes) with a coverage from 2276 to 2290 cm⁻¹ was used to scan the CO₂ absorption transitions. The collimated output of the laser is guided in and out of the discharge chamber through two inserted wedged CaF₂ windows to reduce the CO₂ absorption outside of the discharge along the beam pass. To prevent the disturbance of the gas flow, a 5 mm gap is still maintained between the exit of the discharge and the optical window on both sides. The CO₂ gas in these two volumes is referred in the following discussions as the background gas. A combination of a polarizer and a quarter-waveplate is used to adjust the laser intensity to avoid saturation. Two irises help to prevent potential etalon effects in the optical pass by shielding the back reflection from the beam splitter and the CaF₂ windows. After traversing the discharge chamber, the laser beam is focused onto a DC-coupled photovoltaic detector (Vigo, PVI-3TE-5, bandwidth 1 MHz) by an off-axis parabolic mirror. A narrow bandpass filter (Thorlabs, FB4250-500) and a third iris are mounted in front of the detector to reduce the infrared thermal emission from the discharge. The laser frequency is characterized by a silicon Fabry–Perot interferometer (LightMachinery) with a free spectral range of 0.0176 cm⁻¹ mounted on a flipping mount.

High temporal resolution is achieved by operating the QCL with a slow scan, which can be regarded as a quasi-step-scan mode, as shown in the trigger scheme in figure 1(b). A ramp signal generated from a function generator (Agilent 33 250A) is sent to a commercial laser controller (ILX 3736) to scan the temperature of the QCL with a frequency of $f_1 = 10$ mHz and an amplitude of 5 °C (~ -0.2 cm⁻¹ °C⁻¹). The temperature

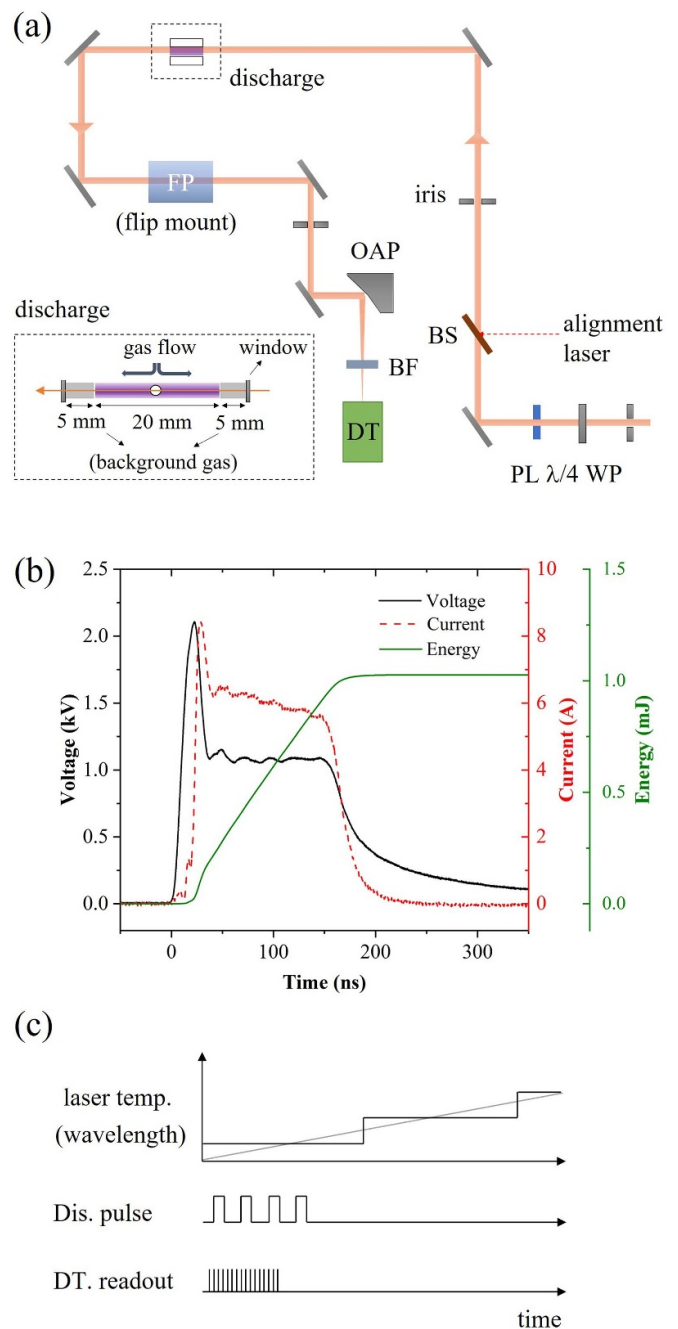


Figure 1. (a) Schematic of the experimental setup, including the discharge chamber and the optical alignment. WP: wave plate, PL: polarizer, BS: beam splitter, OAP: off-axis parabolic mirror, BF: bandpass filter, DT: detector, FP: Fabry–Perot interferometer; (b) voltage, current and coupled energy waveforms for the investigated discharge condition: 10% CO₂ + He at 145 mbar with a repetition rate of 2 kHz and pulse length of 150 ns; (c) schematic view of the laser light path and the trigger scheme for the high temporal resolution measurement.

tuning is adopted as it provides a wider wavelength sweeping range and a smaller intensity variation compared with the current scan. The latter is crucial considering the generally limited dynamic range of the fast IR detector. With such a slow temperature scan, the laser wavelength can be regarded as constant within 20 ms (5 °C/100 s \times 0.02 s = 0.001 °C), considering

the tiny wavelength change ($\sim 2 \times 10^{-4} \text{ cm}^{-1}$) within this time period. For each wavelength step, the temporal profile of 40 ($f_p = 2 \text{ kHz}$) repeated discharge pulses are acquired and averaged in the data post-processing. The light intensity from the detector is read out by an oscilloscope (PicoScope 5444B) with a vertical resolution of 14-bit. The temporal resolution of the measurements is limited by the detector bandwidth. It is also restricted by the discrete choice of sampling rates provided by the oscilloscope. The chosen sampling rate, 666.7 kS s^{-1} , corresponds to a sample interval of $1.5 \mu\text{s}$ that is close to but does not exceed the temporal resolution of the detector. Although this resolution makes it impossible to obtain the evolution of the excitation within the short discharge phase, the achieved temporal resolution of $1.5 \mu\text{s}$ is still high enough to capture the excitation/deexcitation processes in the afterglow (in the order of $100 \mu\text{s}$). To achieve a temporal resolution that would allow the investigation of both phases, a faster detector and a complex sampling scheme are needed. A measurement series is performed in the following procedure:

- Measure the incident laser intensity I_0 by purging the chamber with pure He at 145 mbar;
- measure the wavelength tuning property by inserting the etalon;
- measure the transmitted light I_t with the desired CO_2/He mixture at 145 mbar with discharge turned on.

With all three spectra, the spectrally and temporally resolved CO_2 absorption can be processed and reconstructed. Since each spectrum takes 100 s, the total acquisition time for one measurement is around 5 min. Additionally, one more spectrum measured with the desired gas mixture before turning on the discharge could help to get a self-calibration for the CO_2 concentration and collisional broadening coefficient, but it is not a must for each measurement. Also, it should be noted that since the laser intensity and frequency are measured individually, the temperature tuning signal is always monitored for synchronization.

3. Theoretical analysis

3.1. Calculation of CO_2 absorption spectrum under non-equilibrium condition

Unlike the conventional tunable diode laser absorption spectroscopy (TDLAS), which uses the integrated areas or broadenings of two individual lines to infer gas temperature and species concentration, fitting a broadband absorption spectrum with several transitions is necessary in this paper to obtain the multiple temperatures (T_{rot} , T_{v1} , T_{v2} , and T_{v3}) and concentration of CO_2 . For the fitting this spectrum first needs to be calculated as a function of the various temperatures.

The calculation algorithm is implemented based on the HITEMP-2010 database [35], which contains the line-by-line information of CO_2 for 12 isotopes and hot bands up to $v_3 = 6$. The notation of a vibrational state in this paper follows the Herzberg rule [36] with an extra ranking index r to classify the

Fermi resonating group ($v_1 v_2^{l_2} v_3 r$). ($r = 1, 2, 3, \dots, v_1 + 1$; $r = 1$ denotes the highest vibrational level within a resonating group). In this terminology system there only exist transitions with $l_2 = v_2$ since all other levels ($v_1 v_2^{l_2} v_3$) ($l_2 \neq v_2$) are resonated with $((v_1 - l_2/2) l_2^{l_2} v_3)$ levels, although theoretically l_2 , representing the contribution of bending mode to the angular rotation, can take values from $v_2, v_2 - 2, \dots$. The absorbance $A(\nu)$ or fractional absorption (used when the absorption is too strong or even saturated), as described by the basic Beer-Lambert Law, can be calculated as follows,

$$A(\nu) = -\ln(I_t(\nu)/I_0(\nu)) = S(T) \cdot p \cdot x_{\text{CO}_2} \cdot l \cdot \sigma(\nu), \quad (1)$$

where $I_t(\nu)$ and $I_0(\nu)$ are the transmitted and incident light intensities, respectively. p and l are the total pressure (atm) and optical length (cm), determined by the experimental conditions. x_{CO_2} is the mole fraction of the CO_2 and $\sigma(\nu)$ is the line profile.

The linestrength $S(T)$ ($\text{cm}^{-1}(\text{atm} \times \text{cm})^{-1}$) at a certain temperature can be calculated from the Einstein coefficients from HITEMP as shown in [17, 27] with special attention paid to the definition of all derived parameters [37]. A better and easier way of calculating the linestrength at a specific temperature or temperature set $T = (T_{v1}, T_{v2}, T_{v3}, T_{\text{rot}})$ under non-equilibrium conditions is the rescaling method,

$$S(T) = S(T_{\text{ref}}) \cdot \frac{f''(T)}{f''(T_{\text{ref}})} \cdot \left[\frac{1 - e^{-\Delta E/k_B T}}{1 - e^{-\Delta E/k_B T_{\text{ref}}}} \right], \quad (2)$$

where $f''(T)$ is the fraction of population in the lower state at a specific temperature, ΔE is the energy difference of the upper and lower state and can be obtained from the HITEMP database. $S(T_{\text{ref}})$ is the standard linestrength listed in HITEMP at a reference temperature of $T_{\text{ref}} = 296 \text{ K}$. In this approach, all the inherent constants associated with a specific transition are canceled out in the rescaling method. Only the terms that represent the rescaling factor due to the number density (second term in equation (2)) and stimulated emission (last term) at the target and reference temperature still remain. Therefore, the calculation of the CO_2 absorption spectrum is simplified to the calculation of the number density $f''(T)$.

To calculate the fraction of population f'' under non-equilibrium conditions, the total energy of a specific level ($v_1 v_2^{l_2} v_3 r J$) should be partitioned into different vibrational and rotational modes and scaled with corresponding temperatures,

$$f'' = f_{v1} \cdot f_{v2} \cdot f_{v3} \cdot f_J \quad (3)$$

where f_J and f_{v_i} are the fractions of the population in the pure rotational and vibrational dimensions. Considering the fast translation-rotation processes (T-R) process (with a characteristic time in the order of tens of ns under our conditions), the rotational temperature is in equilibrium with the gas temperature T_g and the rotational distribution function always follows the Boltzmann distribution. The vibrational distribution can be well described by a Treanor distribution [38] especially for the v_3 mode, which has a faster V-V exchange rate than that of V-T. Therefore,

$$f_{vi} = \frac{g_{vib,i}}{Q_{vib,i}} \exp\left(-c_2 \left(\frac{E_{h,i}}{T_{vib,i}} + \frac{E_{a,i}}{T_{rot}}\right)\right)$$

$$f_J = \frac{g_i \cdot g_s \cdot (2J+1)}{Q_{rot}} \exp\left(-c_2 \cdot \frac{E_{rot,J}}{T_{rot}}\right), \quad (4)$$

where $g_{vib,i}$ is the degeneracy of each vibrational mode and equals 1 for the ν_1 and ν_3 modes. For the doubly degenerate bending mode ν_2 , since the vibrations in two orthogonal planes have the same vibrational energy and any linear combination of the two eigenfunctions is also an eigenfunction of the same energy level, the degeneracy is $\nu_2 + 1$. $E_{h,i} = \nu_i \omega_i$, and $E_{a,i} = -\nu_i(\nu_i - 1)\omega_e x_e$ are the harmonic and anharmonic components of the vibrational energy, which are scaled with the vibrational temperature T_{vi} and the rotational temperature T_{rot} in the Treanor distribution, respectively. ω_i and $\omega_e x_e$ are derived from the vibrational constants from paper [39], similarly as in [17, 27]. As for the rotational term, the g_i and g_s are the rotational state-independent and state-dependent nuclear spin statistical weights. g_s depends on the total spin of the interchanged identical nuclei in a molecule and will cause the vanishing of symmetric (or asymmetric) rotational state and thus should be discussed accordingly for different CO₂ isotopologues [37]. The partition sums, $Q_{vib,i}$ and Q_{rot} , are separately calculated under non-equilibrium conditions by numerical summation of all the vibrational and rotational levels with a truncation at $\nu_1 = 20$, $\nu_2 = 43$, $\nu_3 = 13$, and $J = 150$ [40]. The truncation is validated by checking the convergency of $Q_{tot} = Q_{rot} \cdot Q_{vib,i}$ up to 3000 K (>99.93%) and by comparison with the tabulated database from [41] under equilibrium conditions.

The line profile $\sigma(\nu)$ (cm⁻¹) is described by a Voigt profile with consideration of the line-dependent Doppler and collisional broadenings. To accelerate the simulation and thus the fitting algorithm, the direct summation formed Voigt profile, proposed by Liu *et al* [42] is used with good accuracy. At our experimental conditions (T_g close to room temperature), the half-width at half-maximum of the Doppler broadening determined by the gas temperature, δ_G , is around 0.002 cm⁻¹ and is one order of magnitude smaller than that of the collisional broadening calculated as follows,

$$\delta_c(p, T) = p \cdot \left[\left(\frac{T_{ref}}{T}\right)^{n_{CO_2}} \cdot \gamma_{CO_2} \cdot x_{CO_2} \cdot \left(\frac{T_{ref}}{T}\right)^{n_{He}} \times \gamma_{He}(1 - x_{CO_2}) \right], \quad (5)$$

where γ_{CO_2} and γ_{He} are the self-broadening and He-broadening coefficient of CO₂ at reference condition ($T_{ref} = 296$ K and $p_{ref} = 1$ atm) and n_{CO_2} and n_{He} are the corresponding temperature exponents. Due to the lack of detailed line-by-line data, n_{CO_2} and n_{He} are assumed to be equal to n_{air} from HITEMP database, which is reasonable considering the low gas temperature in our experimental condition. The collisional broadening coefficient γ_{He} , is calculated based on the tabulated data γ_{air} from HITEMP with $\gamma_{He} = q \cdot \gamma_{air}$ assuming the same dependence on rotational quantum J but a global quenching factor to correct the difference between He and air. The quenching factor q will be measured and discussed later.

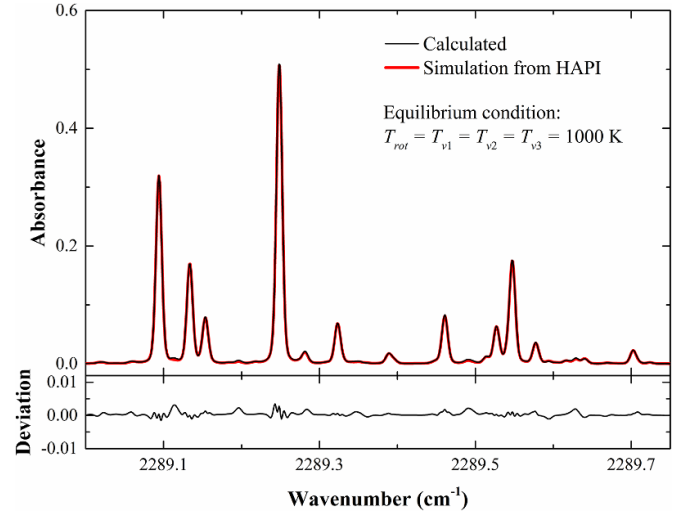


Figure 2. Comparison of the calculated absorption with HAPI at equilibrium condition ($T_{rot} = T_{\nu_1} = T_{\nu_2} = T_{\nu_3} = 1000$ K) for 10% CO₂, $p = 0.03$ atm and $l = 1$ cm.

The collisional broadening due to the potential dissociation products O₂ or CO are ignored in our experiments considering the low dissociation rate and low CO₂ concentration.

3.2. Validation of the simulation under both equilibrium and non-equilibrium conditions

The code simulating the absorption spectrum is validated by comparisons with the equilibrium CO₂ absorbance calculated with HAPI [43] (HITRAN Application Programming Interface to calculate equilibrium spectra) and measured non-equilibrium absorption spectrum from the literature [17, 44].

Figure 2 shows a comparison of the equilibrium absorbance for pure CO₂ around 2289.5 cm⁻¹ calculated from HAPI with $T = 1000$ K and the established non-equilibrium simulation code with $T_{rot} = T_{\nu_1} = T_{\nu_2} = T_{\nu_3} = 1000$ K. The moderate pressure, $p = 0.03$ atm, is chosen to ensure a comparable contribution of the Gaussian and the Lorentzian broadening, thus the broadening calculation and the line profile could also be inspected. Furthermore, since the total energy and the total internal partition sums used in HAPI are calculated *ab initio* [41], the perfect agreement between these two simulations also suggests the accurate calculations of the total energy and of the partition function in the rescaling model. It should also be noted that when calculating the equilibrium spectra, the energies of the Fermi-resonant levels are additionally corrected by calculating the Fermi coupling off-diagonal elements as shown in [39, 45].

To further validate the splitting of the total energy of a specific energy level into different rotational and vibrational modes in the proposed simulation code, the experimental transmittance under non-equilibrium conditions from the literature [44] is re-investigated and fitted with our fitting codes. Figure 3 shows the measured fractional absorption spectrum from [44] with a mixture of 10% CO₂, 38% N₂, and 52% He at 15 Torr around 2284.4 cm⁻¹. Owing to the relatively low

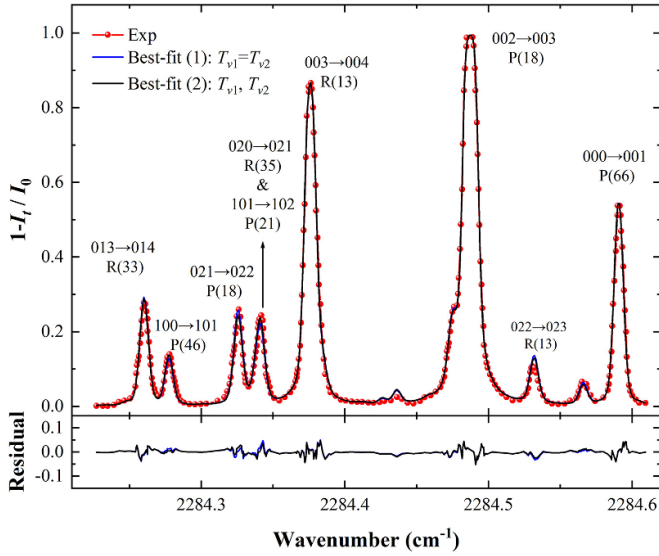


Figure 3. Fit to a non-equilibrium CO₂ absorption from the literature [44]. Each peak is denoted as ($v_1 v_2 v_3$) with l and r omitted to reduce the complexity of the notation.

pressure, the detected absorption peaks are well separated. The corresponding dominant transitions are identified and labeled to indicate the dependence of the peak intensities on the different vibrational and rotational temperatures. Two different fits are made. For the first one (blue curve in figure 3) $T_{v1} = T_{v2}$ is assumed, whereas for the second one (black curve) T_{v1} and T_{v2} are considered independent. As can be seen, both fitting results agree very well with the experimental results. The values for the temperatures obtained from the fits are: $T_{rot} = 495 \pm 9$ K, $T_{v1} = T_{v2} = 508 \pm 7$ K, $T_{v3} = 2634 \pm 60$ K for the first case and $T_{rot} = 498 \pm 9$ K, $T_{v1} = 522 \pm 10$ K, $T_{v2} = 500 \pm 8$ K, $T_{v3} = 2658 \pm 63$ K for the second case.

Several conclusions can be made based on these fitting results. Firstly, the approximate equality of the fitted vibrational temperatures T_{v1} , T_{v2} for the second case and $T_{v1,2}$ in case (a) corresponds well with the conclusion obtained from a Boltzmann plot in [44]. This confirms the assumption used in the following discussion that $T_{v1} = T_{v2}$ due to the strong coupling between the symmetric stretch and bending modes, i.e. Fermi resonance [17, 46]. Secondly, although no detailed temperatures were provided for this example transmittance in [44], the fitted temperatures match well with those from [17, 27, 47] with a similar fitting algorithm, which again verifies the accuracy of the simulation code and partition of ro-vibrational energy. Thirdly, it is also worth noticing that the relatively large fitting uncertainty (calculated with 95% confidence bounds), is attributed to the non-ideal selection of wavelength range, i.e. insufficient energy gap, and the almost saturated strong absorptions, both of which reduce the sensitivity of the detected absorbance to the gas temperature or, equivalently, the concentration. This is also one of the reasons why in addition to this example absorbance, several other wavelength intervals, from 2140 to 2310 cm^{-1} , were needed to be scanned in [44] to obtain accurate rotational and vibrational temperatures. Therefore, a well-selected wavelength is

essential for the accuracy of the results when the total scan range is limited.

3.3. Transition (wavelength) selection and fitting strategy

Considering the limited scan range of a single-mode mid-infrared laser, a well-selected wavelength range is needed for the simultaneous determination of the multiple temperatures and the concentration. Except for a reasonable absorption strength, which should be neither too small to ensure a good signal-to-noise ratio, nor so big to cause an absorption saturation and thus be less sensitive to the fitting parameters, some other nontrivial rules need to be taken into account while selecting the wavelength window. Since there are at least five parameters T_{rot} , T_{v1} , T_{v2} , T_{v3} and x_{CO2} to be determined, at least five independent equations or constraints are required to avoid an undetermined system. The following guidelines were used when selecting the wavelength range in this work.

- To obtain accurate T_g or T_{rot} : one pair of lines from the same vibrational level (better to be the ground vibrational level) with a difference in rotational level J as large as possible should be included;
- to obtain accurate T_{vi} : at least one transition from each vibrational mode, i.e. symmetric stretching ($v_1 x^x xx$), symmetric bending ($x v_2^x xx$), and asymmetric stretching ($xx^x v_3 x$) with $v_1, v_2, v_3 > 0$ should be included;
- to increase the reliability of the individual vibrational temperatures, transitions with multiple quanta excited, e.g. $v_1 v_2^x xx$, v_1 and $v_2 > 0$ are recommended.

Based on the above-mentioned guidelines, a wavelength window of $\sim 1 \text{ cm}^{-1}$ near 2289 cm^{-1} is chosen with all noticeable transitions in that range listed in table 1. The transitions are split into different groups based on their distinct characteristics. For example, all transitions labeled by a number from '0' \sim '5' are the lines that have a measurable absorption at room temperature. These lines can be detected without a discharge as a benchmark of the wavelength window. The transitions that are sensitive to the vibrational temperature of the symmetric (T_{v1} or T_{v2}) and the asymmetric modes (T_{v3}) are marked by lowercase and uppercase alphabetic characters, respectively.

To further demonstrate the high sensitivities of the selected transitions to different temperatures, a simplified energy level scheme for the lower ro-vibrational states of the selected transitions are plotted in figure 4(a) with the respective vibrational state marked as a grey line below and the rotational quantum J in the bracket. Peaks '0' and '3', both belonging to transitions to the ground state, are a perfect line pair for the rotational temperature measurement due to their large J difference up to 56 and comparable intensities (see figure 4(b)). Furthermore, in addition to the coverage of the transitions from all three vibrational modes, the selected wavelength window also includes absorption lines that have a lower level with multiple vibrational modes excited, e.g. 'b', 'B' and 'C'. Therefore, the population density of these levels depends on a combination of the vibrational temperatures. Then the fitting quality of these

Table 1. Spectroscopic parameters for the selected CO₂ transitions from HITEMP 2010 [35].

Label	Frequency (cm ⁻¹)	Vib.	Rot.	Energy (cm ⁻¹)
0	2288.784	00 ⁰ 01	R6	16.39
1	2289.094	01 ¹ 01	P51	1702.40
2	2289.134	02 ² 01	P39	1945.79
3	2289.249	00 ⁰ 01	P62	1522.16
4	2289.396	01 ¹ 01	R24	883.18
5	2289.548	10 ⁰ 02 ^a	P42	1990.11
a	2289.323	03 ³ 01	P26	2278.63
b	2288.671	11 ¹ 01	P29	2416.42
c	2288.476	10 ⁰ 01	P42	2092.49
A	2289.461	00 ⁰ 11	P39	2952.76
B	2289.578	01 ¹ 11	P26	3276.04
C	2288.601	01 ¹ 11	P27	3297.41

^a Notation with consideration of Fermi-resonance. Theoretically, it belongs to the vibrational level (02⁰0) as shown in the energy level scheme in figure 4(a).

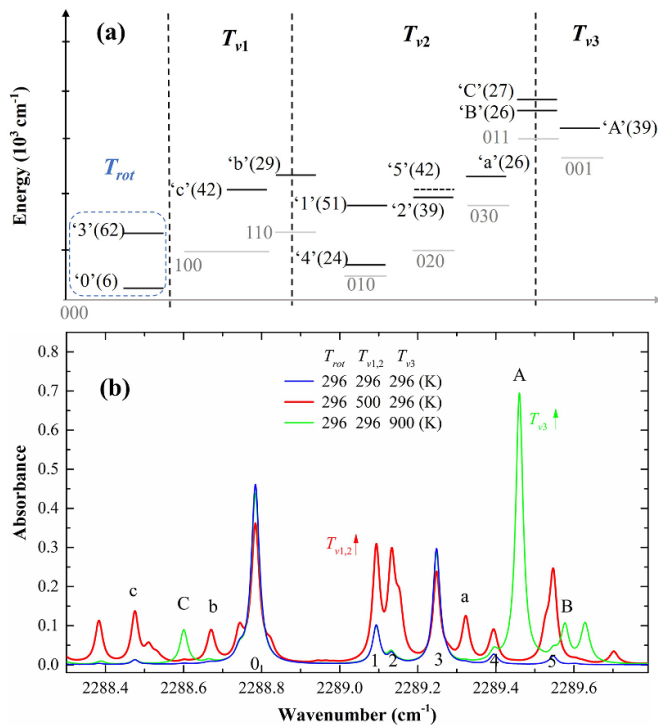


Figure 4. (a) Simplified energy level scheme for the transitions used in this paper and the corresponding sensitivity to different vibrational and rotational temperatures. The label of each peak is denoted as ($v_1 v_2 v_3$) with l and r omitted to reduce complexity. (b) The simulated absorption spectra in the selected wavelength range at room temperature and at non-equilibrium conditions with $p = 145$ mbar, 10% CO₂, $l = 2$ cm.

peaks is a measure of the reliability of the determination of the individual vibrational temperatures. Figure 4(b) compares also the calculated absorption in the target wavelength range under our experimental condition (10% CO₂, $p = 145$ mbar, $l = 2$ cm) at room temperature and at elevated vibrational temperatures. As can be seen, in addition to a reasonably strong absorption intensity for all peaks, the strong sensitivity of the target transitions to the different temperatures is clearly

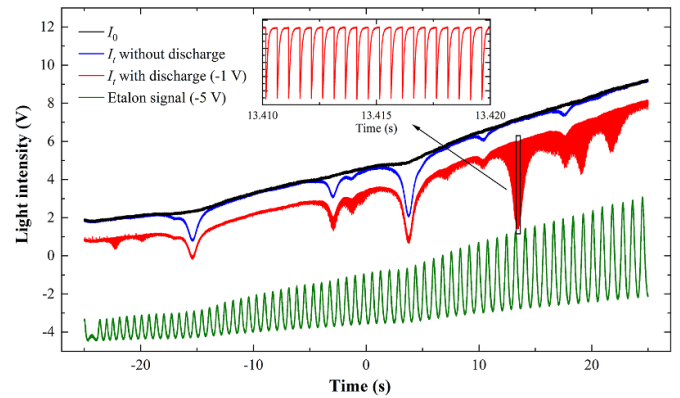


Figure 5. Example of the detected spectra for a time series measurement. The QCL is scanned by temperature with $f = 10$ mHz. The discharge is operated with 10% CO₂ + He at 2 kHz with a voltage of 3 kV, current of ~ 6 A, and a pulse length of 150 ns. The light intensities of I_t with discharge and the etalon signal are shifted vertically for clarity. The inset is an example zoom of I_t within a constant wavelength step showing the variation of absorbance within the discharge afterglow.

observed. Consequently, the chosen wavelength window is good enough to provide the desired sensitivity to the various parameters of interest.

4. Results and discussions

Figure 5 shows a representative example of the detected spectra required for a time series measurement. As shown by the etalon fringes, the QCL is tuned over 1.14 cm⁻¹ ($= 65$ fringes $\times 0.0176$ cm⁻¹) within 50 s to probe all the transitions under investigation. To obtain the absolute frequency, firstly the signal from the etalon is averaged over a period of 20 ms. Then the positions of the fringe peaks are read out and fitted by a third-order polynomial. The absolute wavelength is obtained by using the position of the absorption peak at 2288.78 cm⁻¹.

The baseline I_0 shows tiny absorption features, especially around peaks ‘0’ and ‘3’. They originate from the CO₂ gas outside the chamber i.e. the one unavoidably present in the ambient lab atmosphere (~ 400 ppm, 1 atm, absorption path around 2 m). They contribute equally both to I_0 and to the transmitted light intensity I_t . Therefore, they cancel out when calculating the absorbance of the discharge. Beside the three spectra required for a time series measurement, the spectrum recorded with the desired gas mixture before turning on the discharge is also included in figure 5. Compared with the smooth incident light intensity, I_0 , absorption peaks that have detectable intensity at room temperature and marked as 0–5 in section 3.3 are observed with the CO₂ gas mixture as I_t . This spectrum allows an experimental estimation of the quenching factor q , ensures no systematic error in the gas mixture, and also provides a closer inspection of the stability of the whole system. The transmitted light intensity with discharge is shown in red. Prominent differences are observed in comparison to the one without a discharge. As can be seen, transitions from high vibrational levels, marked as alphabetic characters in section 3.3 appear when the discharge is turned on. These peaks appear shaded in the figure due to their strong change within the discharge afterglow, as shown in the inset in figure 5. The recorded spectra then provide a temporally resolved measurement of the CO₂ absorption in the afterglow of the nanosecond discharge.

4.1. Measurement of collisional broadening coefficient $\Upsilon_{\text{He-CO}_2}$ under equilibrium conditions

Since the collisional broadening of CO₂ is dominant at our experimental pressure and 90% of the collisional partners are He atoms, it is important to have an accurate collisional coefficient of CO₂ with He, γ_{He} . The arbitrary assumption that γ_{He} equals γ_{air} listed on the HITRAN or HITEMP database due to the lack of detailed data from literature, will result in a visible discrepancy in the best-fit spectrum and an overestimation of the finally fitted CO₂ concentration due to the overestimation of the broadening effect. Here, we conducted an experimental measurement of q by checking the CO₂ absorption spectrum under equilibrium conditions.

Figure 6 shows the measured and best fitted CO₂ absorbance within the target range under equilibrium conditions. The red circles are the measured spectrum with 10% CO₂ + He at a pressure of 145 mbar without discharge. The best-fit spectrum with collisional coefficient q as an extra fitting parameter is shown in black. As can be seen, perfect agreements are observed for all peaks and the best fit parameters are as follows, $T_{\text{rot}} (= T_{v1} = T_{v2} = T_{v3}) = 297.5 \pm 0.2$ K, $x_{\text{CO}_2} = 9.8 \pm 0.1\%$ and $q = 0.80 \pm 0.01$. The uncertainties given here and in the following discussions include only the uncertainty calculated with 95% confidence bounds from the fitting procedure. The best-fit gas temperature $T_{\text{rot}} = 297.5 \pm 0.2$ K is a reasonable room temperature in the lab and the best-fit CO₂ concentration also agrees well within uncertainty with the preset value. In addition, this overall quenching factor $q = 0.80 \pm 0.01$ obtained from the fitting yields a collisional broadening coefficient

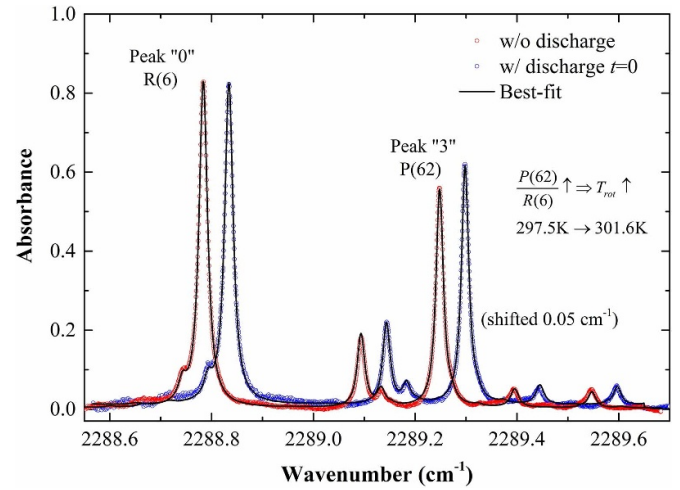


Figure 6. Absorbance of the CO₂ gas mixture without discharge (red symbols) and before the discharge pulse ($t = 0 \mu\text{s}$) (blue symbols) for the target scan range. The blue curve is shifted horizontally by 0.05 cm^{-1} for clear comparison.

$\Upsilon_{\text{He}} = 0.062 \text{ cm}^{-1} \text{ atm}^{-1}$ for the strong absorption peak $R(6)$, which agrees within the uncertainty with the measured value from the literature [48]. The collisional broadening coefficients of CO₂ with He for other target transitions, which are not observed at room temperature, are all rescaled with this q factor, assuming the same rotational quantum J dependence as with air.

The detected CO₂ absorption spectrum and its best-fitting with the same gas mixture but at a slightly elevated gas temperature under equilibrium is also included in figure 6. This spectrum is obtained while running the discharge in an effectively single-pulse mode by increasing the gas flow rate to 400 sccm. Under such conditions, the gas residence time is less than the time between two consecutive pulses, thus the absorption path between the chamber windows is filled with fresh gas mixture before each discharge pulse. The best-fit gas temperature and CO₂ concentration are $T_{\text{rot}} = 301.6 \pm 0.2$ K and $x_{\text{CO}_2} = 9.8 \pm 0.1\%$. The gas temperature is slightly higher than the one measured without the discharge operating ($T_{\text{gas}} = 297.5$ K). The reason for this slight discrepancy is probably heating from the electrodes whose temperature probably changes due to the operation of the discharge. As can be seen in figure 6, even with a temperature increase of only 4.1 K, the intensity of peak ‘3’ that belongs to a high rotational state, and thus the ratio of peak intensity between peak ‘3’ and ‘0’, increase notably due to the large energy difference between these two lines. This demonstrates the high accuracy of this method and confirms the good selection of the wavelength window.

In addition to inferring the collisional factor q , the stability of the measurement method and optical system can be evaluated with the absorption spectrum measured without discharge. By recording the pulse signal while the high voltage power supply is off, the temporally resolved absorbance of the neutral CO₂ gas mixture can be reconstructed with the same procedure as in the measurement with discharge. By fitting the time-resolved absorbance of the CO₂ gas mixture without

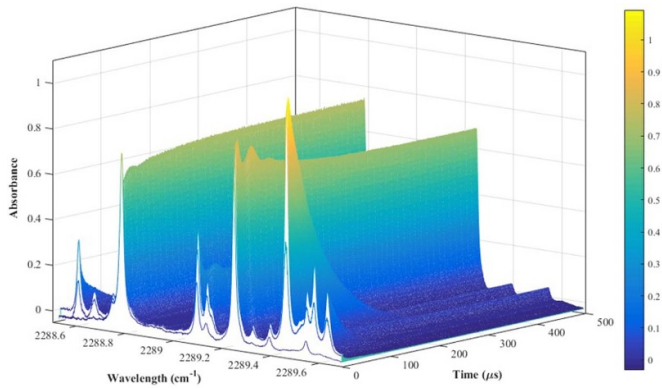


Figure 7. Time evolution of the measured absorbance in the afterglow of the nanosecond discharge. The discharge is operated with 10% CO₂ + He at 145 mbar with a frequency of 2 kHz, a voltage of 3 kV ($I \sim 6$ A), and a pulse length of 150 ns.

discharge, the robustness of this method could be assessed. The averaged best-fit rotational temperature, CO₂ concentration and quenching factor over 500 μ s are 297.50 K, 9.794% and 0.799, with a standard deviation of 0.04 K, 0.007% and 0.001, respectively. It is clear that the standard deviation of the background is smaller than the fitting uncertainty within the 95% confidence bound error of the fitting process, which suggests the good stability of the experimental system and the method over time.

4.2. Temporally resolved measurement

Figure 7 presents the temporally and spectrally resolved absorption of CO₂ in the nanosecond CO₂-He discharge at 145 mbar with a frequency of 2 kHz, voltage of 3 kV and a pulse length of 150 ns. As can be seen, immediately after the discharge pulse, the peaks from the excited vibrational states appear and rise dramatically within the first 3 μ s, which suggests a distinct vibrational excitation of CO₂ due to the discharge. After that, a clear decay is observed for all these peaks. In contrast, the change in peaks 0 and 3 from the ground vibrational state is relatively moderate during the whole process, except for an oscillation within the first 100 μ s, indicating a mild variation in the rotational temperature. Through the fitting of the temporally resolved absorption spectra, the evolution of the CO₂ rotational and vibrational temperatures can be obtained.

Several representative absorption spectra at different time points are shown in figure 8, together with the corresponding best-fit. At $t = 0 \mu$ s, just before the next discharge pulse, local thermal equilibrium is observed along the whole absorption pass, including both, discharge volume and background. The best-fit temperature is $T_{rot} = T_{v1,2} = T_{v3} = 311.1 \pm 0.2$ K, suggesting a negligibly small gas heating in this highly non-thermal nanosecond discharge. The best-fit CO₂ concentration reduces to $9.4 \pm 0.1\%$, indicating a dissociation degree of only 4% of the CO₂ gas. This CO₂ dissociation degree is close to the value reported from a pin-to-sphere configured nanosecond discharge [5, 9] with a similar specific energy

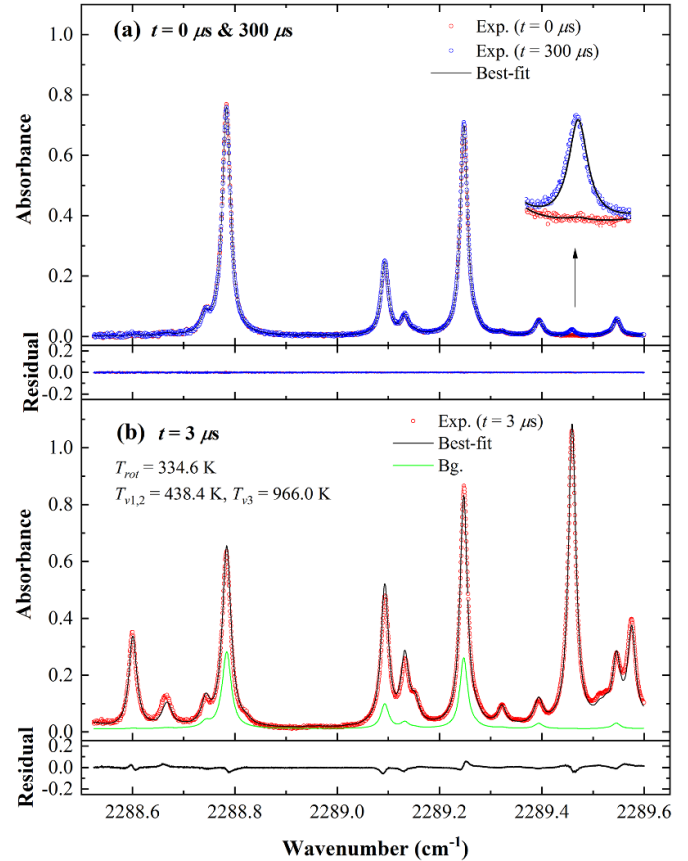


Figure 8. Examples of fitted absorption spectra together with the corresponding fitting residual for a discharge of 10% CO₂ + He with a frequency of 2 kHz, voltage of 3 kV and a pulse length of 150 ns. (a) Before discharge pulse $t = 0 \mu$ s and $t = 300 \mu$ s; (b) $t = 3 \mu$ s when T_{v3} reaches the maximum.

input of 0.9 eV/molecule (calculated with mean pulse energy around 1 mJ, figure 1(b)). Considering the low gas flow rate and the interchange between the discharge volume and the background, the temperature and CO₂ concentration of the background gas remain unchanged during the entire afterglow. This allows to account for the contribution of the background to the absorption spectra obtained in the afterglow by generating the background spectrum using the temperature and CO₂ concentration obtained at $t = 0 \mu$ s. The green line in figure 8(b) depicts this spectral contribution of the background gas to the final line-of-sight spectrum. Although the optical length of the background gas accounts for around 50% of the absorption length, the background has limited influence on the final fitting results due to its small contributions to the peak intensities. Furthermore, it has essentially no influence on the determination of the asymmetric vibrational temperature, since the background does not contribute to the peak from which T_{v3} is determined.

The absorption spectrum of CO₂ at $t = 3 \mu$ s, changes dramatically as shown in figure 8(b). All three vibration modes are highly excited, especially the asymmetric stretch mode, as shown by the distinct peak ‘A’. The best-fit temperatures are $T_{rot} = 334.6 \pm 0.6$ K, $T_{v1,2} = 438.4 \pm 1.2$ K and $T_{v3} = 966.0 \pm 1.5$ K. It is clear to see that good

agreement exists between the measurement and the best-fit in this strongly non-equilibrium condition. The larger residuals compared with those under equilibrium conditions are probably attributed from the less accurate line positions for the higher ro-vibrational states and the calculation of the partition function under non-equilibrium condition. As shown in the temporally resolved absorption profile in figure 7, after $t = 3 \mu\text{s}$ the intensity of the transitions from excited vibrational states decay fast with time and finally reach zero. An example of the measured absorbance at a later phase $t = 300 \mu\text{s}$ is also attached in figure 8(a). In comparison with the spectrum at $t = 0 \mu\text{s}$, all transitions overlap with each other except for peak 'A' that belongs to the vibrational state (001). This suggests that until $t = 300 \mu\text{s}$, T_{rot} , T_{v1} , and T_{v2} have already decayed to the same value as in the equilibrium condition before the discharge pulse, while T_{v3} is still higher than the others. This is also reflected in the best-fit temperatures: $T_{\text{rot}} = 311.9 \pm 0.2 \text{ K}$, $T_{v1,2} = 312.0 \pm 0.4 \text{ K}$ and $T_{v3} = 443 \pm 2 \text{ K}$, indicating a slower deexcitation of the asymmetric stretch mode of CO_2 compared with the symmetric stretch or bending modes, as will be discussed later.

By fitting the overall time-resolved absorbance in figure 7, the evolution of T_{rot} , $T_{v1,2}$ and T_{v3} in the afterglow of the nanosecond discharge can be obtained, as shown in figure 9. It should be noted that during the overall fitting process, no extra assumption or *a priori* constraints are used in the fitting to ensure a self-consistent result, except for the time-invariant parameters for the background CO_2 . As can be seen, before the discharge pulse, $t = 0 \mu\text{s}$, thermal equilibrium is obtained among all degrees of freedom, i.e. translation, rotation, and all three vibration modes. During the 150 ns discharge pulse, the CO_2 molecules get excited by the energetic electrons. Further effort will be made in the future to look into the discharge phase with a temporal resolution of $\sim\text{ns}$ by replacing the detector with one having a larger bandwidth ($>100 \text{ MHz}$). After the discharge pulse, the vibrational temperatures as well as the gas temperature keep increasing and reach their maximum values at around $3 \mu\text{s}$ after the pulse. Pronounced excitation of the asymmetric mode is observed with a peak vibrational temperature of $T_{v3, \text{max}} = 966 \pm 1.5 \text{ K}$, while the excitation of the symmetric one is rather moderate with $T_{v1,2, \text{max}} = 438.4 \pm 1.2 \text{ K}$. This confirms the preferential excitation of the asymmetric stretch mode of CO_2 , as reported with different gas mixtures in experiments [17, 27] and simulations [6, 7]. In addition, the elevation in the gas temperature is even more insignificant with a peak value of only $334.6 \pm 0.6 \text{ K}$. This low gas temperature is shown to be very desirable for CO_2 dissociation since it helps to minimize both the recombination process ($\text{CO} + \text{O} + \text{M} \rightarrow \text{CO}_2 + \text{M}$) and the deexcitation of the higher vibrational states, which may enhance the most energy-efficient pathway of CO_2 dissociation (i.e. through the vibrational levels), through VT relaxation considering the strong temperature dependence of both processes [5, 49]. After $t = 3 \mu\text{s}$, all temperatures start to quasi-exponentially decrease towards an equilibrium value $T_{\text{eq}} = 311.1 \pm 0.2 \text{ K}$ before the next discharge pulse. Experimental results also show that this equilibrium temperature increases slightly ($\sim 10 \text{ K}$) with an increase of the pulse length (from 150 to 200 ns) and applied

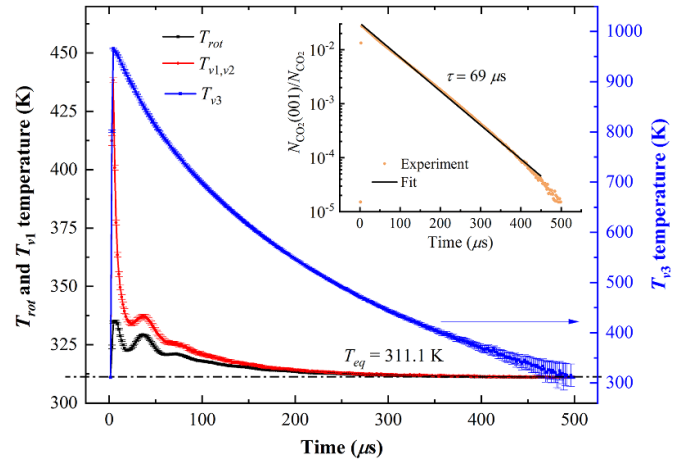


Figure 9. Time evolution of the best-fit rotational temperature and vibrational temperatures in the afterglow of the nanosecond discharge with 10% $\text{CO}_2 + \text{He}$. The discharge condition is the same as that in figure 7. The inset depicts the evolution of the normalized number density (001) state versus time together with the best-fitted exponential decay.

voltage (from 3 to 3.5 kV) due to the increase in the pulse energy. Furthermore, it also can be seen that the symmetric stretching (and bending) modes present a faster decay than the asymmetric mode, due to the generally larger V-V and V-T relaxation cross sections of the symmetric bending modes compared with the asymmetric one [10, 50].

4.3. Deexcitation of the asymmetric mode and acoustic wave perturbation

The inset in figure 9 depicts the time evolution of the number density of the CO_2 asymmetric mode (001) state, which essentially determines the vibrational temperature, T_{v3} , in the broadband spectrum fitting. As can be seen, the number density of CO_2 (001) state closely follows an exponential decay with a time constant of $\tau = 69 \mu\text{s}$. The measured decay constant matches well with the theoretical values $\tau = (\tau_{\text{VT}}^{-1} + \tau_{\text{Wall}}^{-1})^{-1} = 73 \mu\text{s}$ by considering its loss mechanisms of VT transfer with He and the deexcitation at the wall ($\tau_{\text{VT}} \sim 127 \mu\text{s}$ estimated with $\sigma \sim 2 \times 10^{-20} \text{ cm}^2$ at 300 K [50], $\tau_{\text{Wall}} \sim 167 \mu\text{s}$ estimated with a destruction probability of $\gamma = 0.2$ with a Pyrex surface [10]). This suggests that the deexcitation of (001) state in our discharge condition is mainly dominated by the VT transfer with the buffer gas and the deexcitation at the wall. However, for a definitive determination of the leading loss channels, a detailed state-to-state model would be necessary. It will need to account also for the observed low dissociation degree of CO_2 . It should be mentioned that although the vibrational temperature T_{v3} is mainly inferred from the number density of the first vibrational level (001), both experiments and state-to-state simulation [6, 7] have shown a nearly-Boltzmann distribution among the asymmetric mode ($v_3 \leq 5$), which makes the measured (001) state a good representative of the asymmetric vibrational mode.

In addition to the slow decay of T_{v3} with respect to T_{rot} and $T_{v1,2}$, another pronounced feature of the temporally resolved

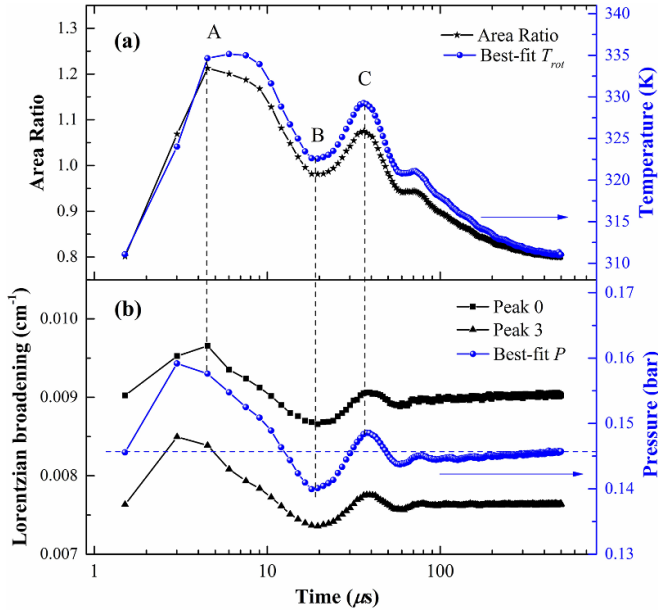


Figure 10. Validation of the best-fit rotational temperature and pressure from the broadband spectrum fitting with the generally used two-line thermometry method (with peaks ‘0’ and ‘3’) in conventional TDLAS.

temperatures is the oscillation in the best-fit T_{rot} and $T_{v,2}$ within the first 100 μs . A similar change is also observed in the best-fit total pressure, as shown in figure 10(b) plotted on a logarithmic scale. Before further discussing the potential origin of this oscillation, the results for the gas temperature and pressure from the broadband spectrum fitting are further validated by the conventional two-line thermometry in TDLAS [29]. It is implemented by fitting the temporally resolved absorption peaks ‘0’ and ‘3’ with a Voigt profile. Since both peaks belong to the same vibrational state (000), the fitted area ratio of these two peaks depends only on the rotational temperature. The Lorentzian broadening components of both peaks are proportional to the total pressure as shown in equation (5) if the slight temperature change is ignored. The area ratio and the collisional broadening from the single peak fitting are shown in figure 10, together with the rotational temperature and pressure results referred from the broadband spectrum fitting. Several conclusions can be obtained: first, the overall ratio of the best-fit Lorentzian broadening of peak ‘0’ and ‘3’ in figure 10(b) is 1.18, which corresponds well with the theoretical ratio of broadening coefficients of these two peaks, suggesting the reliability of the single peak fitting algorithm. Secondly, the good agreements between the time-resolved area ratio and rotational temperature and between the Lorentzian broadenings and total pressure validate the accuracy of the broadband spectrum fitting and the existence of such oscillation.

To further look into this temperature and pressure oscillation process, we estimated the ratio of specific heat capacities of the gas mixture, i.e. $\sim 10\% \text{ CO}_2 + 90\% \text{ He}$ ignoring the slight amount of dissociation products CO or O₂, to be $\gamma_{mix} = 1.583$ ($\gamma_{\text{CO}_2} = 1.275$, $\gamma_{\text{He}} = 5/3$). It should be

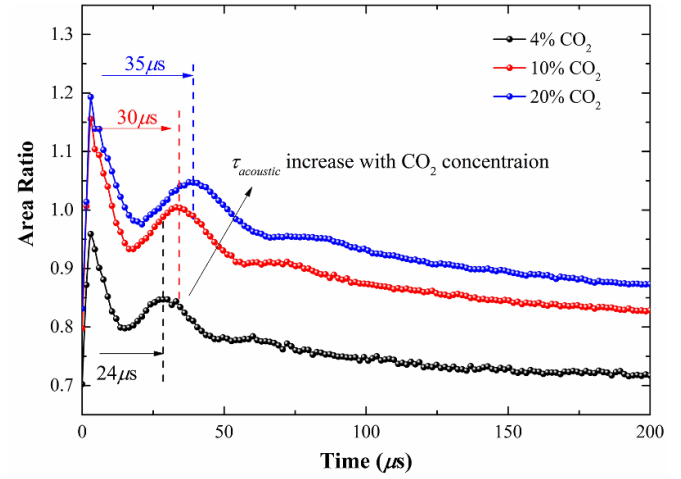


Figure 11. The area ratio of peak ‘3’ and ‘0’ deduced from the single-peak fitting with different CO₂ concentrations.

noted that the ratio of specific heat capacities of CO₂, γ_{CO_2} , used here is calculated at a thermalized averaged gas temperature $T = 330 \text{ K}$. ($C_p = A + B \cdot t + C \cdot t^2 + D \cdot t^3 + E/t^2$, $t = T/(1000 \text{ K})$, with constants A, B, C, E adopted from [51]). Based on γ_{mix} , the pressure changes in $A \rightarrow B$ and $B \rightarrow C$ (figure 10(a)) can be estimated to be 15.2 and 7.9 mbar, respectively, assuming an adiabatic process ($p^{1-\gamma} T^\gamma = \text{const.}$). In fact, the observed pressure changes in the experiments ($p_A - p_B = 17.4 \text{ mbar}$, $p_B - p_C = 8.6 \text{ mbar}$, with p_α being the pressures at the points $\alpha = A, B, C$ read from figure 10(b)), correspond well with the theoretical estimations. The small overshoot in the experiments might be attributed to the underestimation of γ_{mix} caused by a slightly smaller C_p for CO₂, since the asymmetric mode of CO₂ in our experiment is apparently unfrozen, which yields extra degrees of freedom for heat absorption.

Furthermore, as shown in figure 10, the oscillation of the gas pressure shows a damped oscillation with a period around 30 μs , which gives us some hints about its origin. One potential reason might be an acoustic wave produced by the pressure perturbation. The pressure perturbation produced by the discharge propagates with sound speed to the edge of the discharge reactor and finally forms a standing wave in the discharge gap. Since the laser absorption spectroscopy is a line-of-sight technique, the pressure we measured is in fact the averaged pressure along the electrodes. By considering the sound speed in the gas mixture and the geometry of our discharge, the period of the fundamental standing wave mode is $\tau_{acoustic} = \lambda/c_{mix} = 2 \cdot l/c_{mix} \sim 28.5 \mu\text{s}$, where l ($= 10 \text{ mm}$) is the length between two open ends, i.e. the distance between the gas inlet and the discharge boundary, and c_{mix} ($\sim 700 \text{ m s}^{-1}$) is the sound speed in 10% CO₂/He gas mixture. As can be seen, this acoustic time scale agrees very well with the observed period of the pressure oscillation. To further validate this hypothesis, the pressure oscillation was measured with different CO₂/He concentrations as shown in figure 11. A clear increase of the oscillation period is observed with increasing CO₂ concentration due to the decrease of the sound speed in the gas

mixture. The measured oscillation periods, 24, 30, and 35 μs correspond well with the theoretical values, 23.5, 28.5, and 34.2 μs , which supports the origin of the pressure oscillation and also demonstrates the high sensitivity of this measurement method. Acoustic oscillations influence only the gas temperature which is coupled to the rotational temperature. The corresponding oscillations are observed also in $T_{v1,2}$ probably due to a fast V–T exchange for the symmetric modes. However, they are not seen in the temperature of the asymmetric mode, possibly due to the larger energy gap for this mode, making the V–T transfer less efficient. Naturally, these are only qualitative speculations and dedicated studies will be required to unravel the actual kinetics of the V–T transfer.

5. Conclusions

In this paper, we have applied a method to determine the time evolution of CO₂ ro-vibrational excitation with the compact QCL absorption spectroscopy. With a well-selected wavelength window around 2289.0 cm^{-1} and a single QCL operating at continuous mode, the rotational temperature, vibrational temperatures for both symmetric and asymmetric modes, as well as the CO₂ density can be simultaneously determined with both high accuracy and temporal resolution.

The method is further applied to monitor the rotational and vibrational temperatures of CO₂ in the afterglow of a nano-second discharge with a temporal resolution of 1.5 μs . The discharge operates with 10% CO₂ + He at 145 mbar with a frequency of 2 kHz and a pulse length of 150 ns. Experimental results show that both gas temperature and vibrational temperatures keep increasing in the early afterglow and reach the corresponding maximum value at 3 μs . The non-thermal feature and the preferential excitation of the asymmetric stretch mode of CO₂ were clearly observed, with a peak vibrational temperature of $T_{v3,\text{max}} = 966 \pm 1.5$ K, $T_{v1,2,\text{max}} = 438.4 \pm 1.2$ K and $T_{\text{rot}} = 334.6 \pm 0.6$ K. This moderate elevation of gas temperature is shown to be beneficial to the CO₂ dissociation since it helps to minimize the reverse recombination process and the deexcitation of the higher vibrational states. Furthermore, in the relaxation process, the measured number density of CO₂ (001) state presents an exponential decay with a time constant of $\tau = 69$ μs , which is mainly attributed to the VT transfer with He and the deexcitation on the wall. Moreover, within the first 100 μs of the relaxation process, a synchronous oscillation of the gas temperature and the total pressure was observed with a period of 30 μs . It is very likely to be caused by an acoustic wave according to the similar acoustic time scale τ_{acoustic} in our experimental condition and its dependence on the gas components.

Based on these preliminary results, further effort will be made to look into the excitation of CO₂ in the active discharge phase (within the discharge pulse) in combination with a faster detector. Also, the time-dependent measurement of the higher vibrational state in the asymmetric mode is suggested to further check the effect of the vibrational ladder-climbing pathway on the plasma-assisted CO₂ dissociation.

Data availability statement


The data that support the findings of this study are available upon reasonable request from the authors.

Acknowledgments

This work is within the DFG funded SFB1316 Project ‘Transient atmospheric plasmas: from plasmas to liquids to solids’. Yanjun Du acknowledges the financial support from the Alexander von Humboldt Foundation. The authors are indebted to the valuable discussions with Professor Achim von Keudell on the calculation of the non-equilibrium CO₂ spectrum.

ORCID iDs

Yanjun Du  <https://orcid.org/0000-0001-5707-8413>

Tsanko V Tsankov  <https://orcid.org/0000-0002-7937-486X>

Uwe Czarnetzki  <https://orcid.org/0000-0002-5823-1501>

References

- [1] Bogaerts A and Centi G 2020 *Front. Energy Res.* **8** 111
- [2] Bogaerts A, Kozák T, van Laer K and Snoeckx R 2015 *Faraday Discuss.* **183** 217–32
- [3] Fridman A 2008 *Plasma Chemistry* (Cambridge: Cambridge University Press)
- [4] Capezzuto P, Cramarossa F, D’Agostino R and Molinari E 1976 *J. Phys. Chem.* **80** 882–8
- [5] Heijkers S, Martini L M, Dilecce G, Tosi P and Bogaerts A 2019 *J. Phys. Chem. C* **123** 12104–16
- [6] Silva T J, Grofulović M, Klarenaar B L M, Morillo-Candas A S, Guaitella O, Engeln R, Pintassilgo C D and Guerra V 2018 *Plasma Sources Sci. Technol.* **27** 015019
- [7] Grofulović M Silva T, Klarenaar B L M, Morillo-Candas A S, Guaitella O, Engeln R, Pintassilgo C D and Guerra V 2018 *Plasma Sources Sci. Technol.* **27** 115009
- [8] Silva T, Grofulović M, Terraz L, Pintassilgo C D and Guerra V 2018 *J. Phys. D: Appl. Phys.* **51** 464001
- [9] Martini L M, Lovascio S, Dilecce G and Tosi P 2018 *Plasma Chem. Plasma Process.* **38** 707–18
- [10] Terraz L, Silva T, Morillo-Candas A, Guaitella O, Tejero-del-caz A, Alves L L and Guerra V 2020 *J. Phys. D: Appl. Phys.* **53** 094002
- [11] Grofulović M, Klarenaar B L M, Guaitella O, Guerra V and Engeln R 2019 *Plasma Sources Sci. Technol.* **28** 045014
- [12] Klarenaar B L M, Grofulovic M, Morillo-Candas A S, van den Bekerom D C M, Damen M A, van de Sanden M C M, Guaitella O and Engeln R 2018 *Plasma Sources Sci. Technol.* **27** 045009
- [13] Lee W, Adamovich I V and Lempert W R 2001 *J. Chem. Phys.* **114** 1178–86
- [14] Depraz S, Perrin M Y and Soufiani A 2012 *J. Quant. Spectrosc. Radiat. Transfer* **113** 1–13
- [15] Depraz S, Perrin M Y, Rivière P and Soufiani A 2012 *J. Quant. Spectrosc. Radiat. Transfer* **113** 14–25
- [16] Rivallan M, Aiello S and Thibault-Starzyk F 2010 *Rev. Sci. Instrum.* **81** 103111

- [17] Klarenaar B L M, Engeln R, van den Bekerom D C M, van de Sanden M C M, Morillo-Candas A S and Guaitella O 2017 *Plasma Sources Sci. Technol.* **26** 115008
- [18] Klarenaar B L M, Morillo-Candas A S, Grofulovic M, van de Sanden M C M, Engeln R and Guaitella O 2019 *Plasma Sources Sci. Technol.* **28** 035011
- [19] Urbanietz T, Böke M, Schulz-von der Gathen V and von Keudell A 2018 *J. Phys. D: Appl. Phys.* **51** 345202
- [20] Stewig C, Schüttler S, Urbanietz T, Böke M and von Keudell A 2020 *J. Phys. D: Appl. Phys.* **53** 125205
- [21] Morillo-Candas A S, Guerra V and Guaitella O 2020 *J. Phys. Chem. C* **124** 17459–75
- [22] Beyer T, Braun M and Lambrecht A 2003 *J. Appl. Phys.* **93** 3158–60
- [23] Welzel S, Gatilova L, Röpcke J and Rousseau A 2007 *Plasma Sources Sci. Technol.* **16** 822–31
- [24] Marinov D, Lopatik D, Guaitella O, Hübner M, Ionikh Y, Röpcke J and Rousseau A 2012 *J. Phys. D: Appl. Phys.* **45** 175201
- [25] Röpcke J, Davies P, Hamann S, Hannemann M, Lang N and van Helden J-P 2016 *Photonics* **3** 45
- [26] Damen M A, Martini L M and Engeln R 2020 *Plasma Sources Sci. Technol.* **29** 095017
- [27] Damen M A, Martini L M and Engeln R 2020 *Plasma Sources Sci. Technol.* **29** 065016
- [28] Welzel S and Röpcke J 2011 *Appl. Phys. B* **102** 303–11
- [29] Hübner M, Marinov D, Guaitella O, Rousseau A and Röpcke J 2012 *Meas. Sci. Technol.* **23** 115602
- [30] Hübner M, Welzel S, Marinov D, Guaitella O, Glitsch S, Rousseau A and Röpcke J 2011 *Rev. Sci. Instrum.* **82** 093102
- [31] Lepikhin N D, Luggenhölscher D and Czarnetzki U 2021 *J. Phys. D: Appl. Phys.* **54** 055201
- [32] Kuhfeld J, Lepikhin N D, Luggenhölscher D and Czarnetzki U 2021 *J. Phys. D: Appl. Phys.* **54** 305204
- [33] Kuhfeld J, Luggenhölscher D and Czarnetzki U 2021 *J. Phys. D: Appl. Phys.* **54** 305205
- [34] Müller S, Luggenhölscher D and Czarnetzki U 2011 *J. Phys. D: Appl. Phys.* **44** 165202
- [35] Rothman L S, Gordon I E, Barber R J, Dothe H, Gamache R R, Goldman A, Perevalov V I, Tashkun S A and Tennyson J 2010 *J. Quant. Spectrosc. Radiat. Transfer* **111** 2139–50
- [36] Herzberg G 1945 *Molecular Spectra and Molecular Structure II. Infrared and Raman spectra of polyatomic molecules* (London: Van Nostrand)
- [37] Šimečková M, Jacquemart D, Rothman L S, Gamache R R and Goldman A 2006 *J. Quant. Spectrosc. Radiat. Transfer* **98** 130–55
- [38] Treanor C E, Rich J W and Rehm R G 1968 *J. Chem. Phys.* **48** 1798–807
- [39] Suzuki I 1968 *J. Mol. Spectrosc.* **25** 479–500
- [40] Fischer J and Gamache R R 2002 *J. Quant. Spectrosc. Radiat. Transfer* **74** 273–84
- [41] Gamache R R et al 2017 *J. Quant. Spectrosc. Radiat. Transfer* **203** 70–87
- [42] Liu Y, Lin J, Huang G, Guo Y and Duan C 2001 *J. Opt. Soc. Am. B* **18** 666–72
- [43] Kochanov R V, Gordon I E, Rothman L S, Wcislo P, Hill C and Wilzewski J S 2016 *J. Quant. Spectrosc. Radiat. Transfer* **177** 15–30
- [44] Dang C, Reid J and Garside B K 1982 *Appl. Phys. B* **27** 145–51
- [45] Amat G and Pimbert M 1965 *J. Mol. Spectrosc.* **16** 278–90
- [46] Kustova E, Mekhonoshina M and Kosareva A 2019 *Phys. Fluids* **31** 046104
- [47] Pannier E and Laux C O 2019 *J. Quant. Spectrosc. Radiat. Transfer* **222–3** 12–25
- [48] Thibault F, Calil B, Boissoles J and Launay J M 2000 *Phys. Chem. Chem. Phys.* **2** 5404–10
- [49] Kozák T and Bogaerts A 2015 *Plasma Sources Sci. Technol.* **24** 015024
- [50] Stephenson J C, Wood R E and Moore C B 1971 *J. Chem. Phys.* **54** 3097–102
- [51] Chase M W Jr 1998 *NIST-JANAF Thermochemical Tables*, 4th edn (New York: American Institute of Physics)